Available online at www.sciencedirect.com
SCIENCE DIRECT®
Journal of Nuclear Materials 321 (2003) 269–280
journal of nuclear materials
www.elsevier.com/locate/jnucmat

Layer formation on metal surfaces in lead–bismuth at high temperatures in presence of zirconium

Eric P. Loewen [a,*], Hannah J. Yount [b,1], Kevin Volk [b], Arvind Kumar [b]

[a] Idaho National Engineering and Environmental Laboratory, 2525 Fremont Ave, Idaho Falls, ID 83415-3860, USA
[b] Department of Nuclear Engineering, University of Missouri-Rolla, 102 Fulton Hall, Rolla, MO 65409, USA

Received 30 December 2002; accepted 23 May 2003

Abstract

If the operating temperature lead–bismuth cooled fission reactor could be extended to 800 °C, they could produce hydrogen directly from water. A key issue for the deployment of this technology at these temperatures is the corrosion of the fuel cladding and structural materials by the lead–bismuth. Corrosion studies of several metals were performed to correlate the interaction layer formation rate as a function of time, temperature, and alloy compositions. The interaction layer is defined as the narrow band between the alloy substrate and the solidified lead–bismuth eutectic on the surface. Coupons of HT-9, 410, 316L, and F22 were tested at 550 and 650 °C for 1000 h inside a zirconium corrosion cell. The oxygen potential ranged from approximately 10^{-22} to 10^{-19} Pa. Analyses were performed on the coupons to determine the depth of the interaction layer and the composition, at each time step (100, 300, and 1000 h). The thickness of the interaction layer on F22 at 550 °C was 25.3 μm, the highest of all the alloys tested, whereas at 650 °C, the layer thickness was only 5.6 μm, the lowest of all the alloys tested. The growth of the interaction layer on F22 at 650 °C was suppressed, owing to the presence of Zr (at 1500 wppm) in the LBE. In the case of 316L, the interaction layers of 4.9 and 10.6 μm were formed at 550 and 650 °C, respectively.

1. Introduction

The energy demands of the ever increasing human population are escalating and putting extreme demands on Earth's natural resources. Meeting those demands will require innovative energy resources for producing electricity without increasing pollution. Advanced nuclear energy systems offer the means of supplying the world's growing need for energy and a better quality of life. The Idaho National Engineering and Environmental Laboratory (INEEL) is conducting research in advanced reactor development, called Generation IV. One reactor type under consideration is cooled with molten lead (Pb) or molten lead–bismuth eutectic (LBE). The operating range of most molten Pb/LBE reactors is ~550 °C. If the operating temperature of these reactors could be extended from 550 to 800 °C, they could produce hydrogen directly from water. A key safety issue for the deployment of this technology is dissolution or corrosion of the fuel cladding and structural materials by the heavy metal coolant.

Globally, several pump-induced LBE flow loop facilities have been built to study the corrosion rates of various steels and the mass transfer of various elements in LBE up to 550 °C. Some facilities have also conducted stagnant experiments in an attempt to quantify the effect of LBE. Russia (Obninsk) and Germany have run both stagnant and flowing LBE experiments at their facilities at 550 °C. Russia has investigated Optifer IVc, EM10, 1.4948, and 1.4970 in a loop and found limited corrosion and a measurable oxide layer [1]. Germany, at KALLA, studied 316L, 1.4970, and MANET, all

* Corresponding author. Tel.: +1-208 526 9404; fax: +1-208 526 2930.
E-mail addresses: loewep@inel.gov (E.P. Loewen), kumar@umr.edu (A. Kumar).
[1] Tel.: +1-573 341 4747.

0022-3115/$ - see front matter © 2003 Elsevier B.V. All rights reserved.
doi:10.1016/S0022-3115(03)00296-4

alloyed with Al, at the GESA facility in a loop at 550 and 600 °C and found severe corrosion to 316L at 600 °C, but no noticeable attack on the other alloys [2,3]. They also studied Optifer IVc and 1.4970 alloyed with Al in a stagnant environment and found no corrosion [2]. Los Alamos National Laboratory (LANL) studied 316/316L, D9, HT-9, 410, and EP823 in the flowing loop in Obninsk [4]. From the exposures performed in Russia, a kinetic model for the new operational loop was developed. Spain has also performed stagnant tests on 316L and MANET II, revealing logarithmic trends at lower temperatures, and parabolic trends for higher temperatures [5].

This paper describes the interaction layer developed on several martensitic and ferritic steels (HT-9, F22, 410, and 316L) in LBE containing saturated Zr levels at elevated temperatures. The INEEL facility uses a corrosion cell (constructed from Zr pipe) with internal gas injection to induce a loop-like effect. Our choice of US steels includes 316L as a baseline for the mass transfer of nickel. HT-9 was developed for use in the fast reactor project at Argonne National Laboratory West. The 410 has a close resemblance to EP823 which is a Russian alloy used in their submarine LBE reactors and recently studied at Los Alamos. F22 is an iron alloy with a low chromium content (2 wt%). The experiments reported here were designed as an extension of our previous work at higher temperatures in the presence of a zirconium inhibitor. In 1960, James et al. [6] found that a 50 wppm addition of zirconium to bismuth was enough to suppress metallic corrosion. The zirconium nitride formed the protective film at the steel/bismuth interface to inhibit corrosion. Further, they found that carbon was much more effective than nitrogen in the inhibition process by forming ZrC. With Zr as an inhibitor, James et al. [6] reported a reduced corrosion rate by a factor of 40 in bismuth. It is accounted for by the difference in the solubility of iron in LBE. Adding 500 wppm titanium as an inhibitor in a Pb system reduced corrosion as effectively as zirconium in the bismuth system. The protective film in a lead–titanium system is titanium carbide and nitride [6]. This was verified by scientists during early lead corrosion studies [7–10]. We sought to understand the role of Zr to inhibit the corrosion rate in LBE.

2. Experiment

We set up an experimental apparatus to test various materials in LBE at two different temperatures. The experimental conditions and the oxygen control techniques system are explained. Since the mass transfer of elements from the structural metal to the LBE is the major contributor to LBE corrosion the method of measurement is detailed.

2.1. Apparatus

The corrosion test apparatus shown in Fig. 1 achieves loop-type behavior by inducing flow in the riser by injecting gas through a lance. Detailed modeling and measurement of the liquid flow is explained in our previous publications [11,12]. A resistance furnace is used to heat the experimental apparatus to isothermal conditions; see the temperature profile, also in Fig. 1, showing both flow and no-flow conditions. The corrosion cell was constructed of a zirconium (1 wt% Hf) tube. Zirconium has high solubility in LBE. In order to mitigate the dissolution of zirconium into the LBE during the experiments, we pre-oxidized the Zr-tube to create a zirconia (ZrO_2) protective layer. We pre-oxidized the cell by heating the empty Zr-tube to 540 °C and then injected H_20 over 6 h. This produced a tightly adhering black oxide layer of ZrO_2. However, the oxide layer started spalling off during the experiment runs.

A mass spectrometer and O_2-meter measured the gas composition entering and exiting the corrosion cell. The mass spectrometer AERO VAC 2900 sampling system is a turn-key system, consisting of a computer-controlled residual gas analyzer system that controls the heater oven-enclosure for the system, and the 1600 Mass Spectrometer/RGA, which has a two-stage fractionation-free manifold system. The O_2 meter is a Thermox II, which is a self-contained portable analyzer using an electrochemical cell made of ZrO_2 heated to 760 °C, with a lower detection level of 0.1 vppm. The mass spectrometer was limited to a lower O_2 detection level of $\sim$10 vppm. The presence of CO (generated in the corrosion cell) caused the meter to read off-scale low (as would any other flammable gas). By continuously measuring the gas phase during the experiment, we determined the oxygen potential in each corrosion cell using both meters. With submerged gas injection and isothermal conditions, we assume the gas phase oxygen partial pressure to be in equilibrium with the LBE within a range of 10^{-22} to 10^{-19} Pa. We cannot be entirely sure of the oxygen partial pressure in the LBE because of the presence of zirconium, also competing for O_2, which is discussed further in Section 2.3.

2.2. Materials

The growth of interaction layer thickness on different alloy surfaces as a function of time and temperature were measured. Four steel alloys (HT-9, 410, 316L, and F22) and zirconium alloy Zr-4 were subjected to a flowing lead system at 550 and 650 °C for 100, 300, and 1000 h. The chemical composition of each type of steel, as specified by the manufacturer, is presented in Table 1. Metal Samples, Inc., supplied the metallic coupons stamped from rolled sheets and machined into the proper dimensions (3.175 cm OD and 0.32 cm thick).

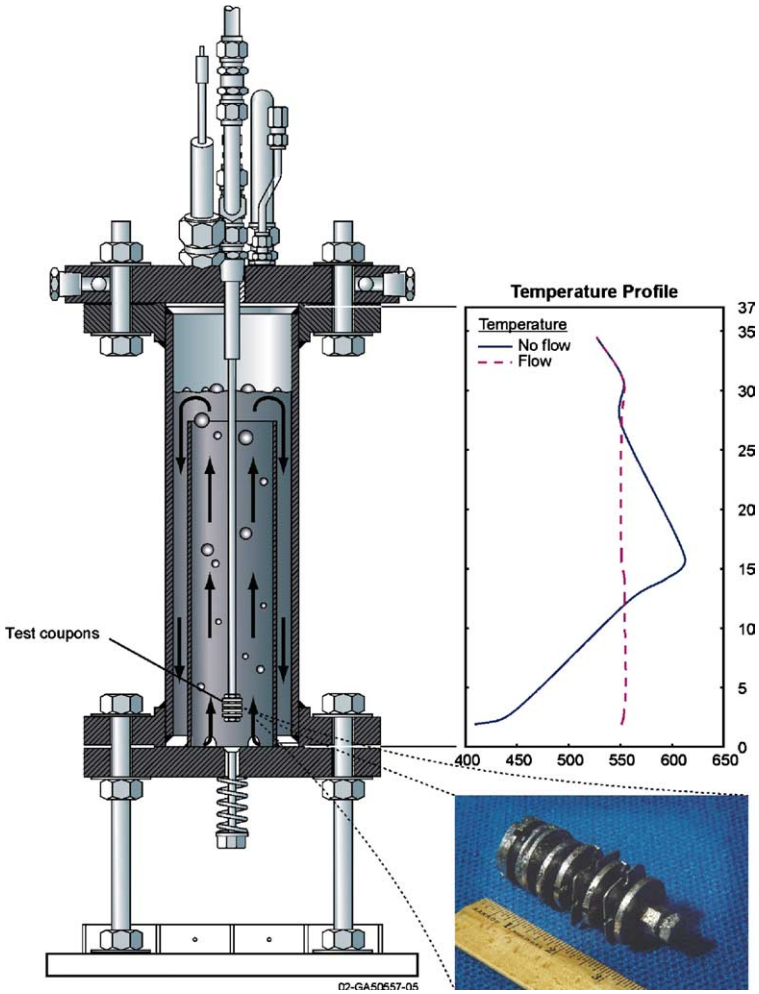

Fig. 1. Schematic diagram of the isothermal gas-lift apparatus used for corrosion resistance testing of various structural materials in heavy liquid metals. A typical axial temperature profile is provided along with a picture of alloy samples removed from the LBE.

Stainless steel 410 was cold rolled. F22 was annealed at 900 °C and then 750 °C. The 316L was heat treated at 820 °C and cooled in air. The precise thermal history of HT-9 is not known because it was cut from a non-irradiated fuel channel box from Argonne National Laboratory West. Each coupon was polished on one side to a 0.3-μm mirror finish (except HT-9 due to a nominal thickness of 1.07 mm), allowing a uniform surface finish to quantify the growth of the interaction layer between time and temperature steps. The coupons were fixed onto a lance separated by alumina spacers and inserted, polished side down, into the corrosion cell. Fig. 1 shows a coupon at the end of a lance after 1000 h of exposure in LBE. Tensile coupons were placed on the outside of the inner shroud (LBE down flow area) for the duration of the experiment.

Upon removal from the molten LBE, the coupons were shaken to remove excess liquid LBE. Then, the coupons were cross-sectioned using a diamond saw, mounted in epoxy, and mechanically polished inward to a 0.3-m mirror finish, by using alumina and silicon carbide. Detailed corrosion and interaction morphologies were obtained with a Philips XL, 20-keV electron beam, scanning electron microscope (SEM). (We define the interaction layer as the narrow band between the alloy substrate and the lead–bismuth eutectic solidified on the surface.) The interaction layer differs from a corrosion layer because more processes are measured and observed than simply the corrosion of the metal. Mass transfer and oxidation of materials as well as the effects of inhibitors are observed. Therefore, the interaction layer is all the material between the metal substrate and the coolant in which the aforementioned processes can be analyzed. The entire coupon cross-section was scanned, and detailed measurements were taken at three separate locations that most accurately

Table 1
Chemical compositions of the metal substrates (wt%)

Element	Zr-pipe	HT-9	316L	410	F22
C	0.013	0.2	0.011		0.093
Cr		12.0	16.340	12.54	2.139
Cu			0.340		0.120
Fe	0.13		Balance	Balance	Balance
Hf	2.60				
Mn			1.490	0.68	0.404
Mo		0.1	2.070		0.925
Nb					0.002
Ni		0.55	10.120		0.122
P			0.028		0.006
S			0.015		0.0013
Si			0.570	0.83	0.130
Sn					0.006
V		0.3			
W		0.5			
Zr	Balance				

portrayed the characteristics of that coupon. Energy dispersive X-ray (EDX) analysis was used to analyze the chemical composition of the interaction (corrosion) layers. The M-line was used for both lead and bismuth; the K-line was used for all remaining materials.

2.3. Experimental conditions and oxygen control

Muller et al. [13] recommend that the oxygen level in LBE be bounded as follows:

$$2\Delta_f G^0_{PbO} > RT \ln p_{O_2} > 0.5\Delta_r G^0_{Fe_2O_4}. \quad (1)$$

Further, Li [14] and Lefhalm [15] have examined active control of oxygen in an LBE system using an H_2 and H_2O mixture to control the oxygen partial pressure. They assume that the gas phase above the molten metal is in equilibrium with the partial pressure in the LBE. However, the exchange of oxygen between the gas phase and liquid metal is limited by diffusion. Therefore, the kinetics of this equilibrium is unique for each geometry and must be measured for each LBE system.

The results reported in this paper used INEEL's solid carbon buffer system ($C/O_2/CO/CO_2$) to keep the oxygen between the bounds established in Eq. (1). This INEEL-developed buffer system (with a provisional patent) uses solid and gaseous carbon to control the oxygen level in the LBE. The calculated standard free energy of formation of oxides (HSC Chemistry, version 4.0) as a function of temperature and normalized for one-gram atom of O_2 are presented in Fig. 2. From visual inspection and inductively coupled plasma (ICP) analysis, we suspect very little breakdown of the ZrO_2 layer on the cell surfaces in the zirconium corrosion cell operated at 550 °C. Therefore, oxygen control may be due to the carbon buffer. When the cell was operated at 650 °C, the ZrO_2 layer both inside and outside the cell spalled off, resulting in saturated Zr levels in the LBE and cracking on the outside of the cell. Since the freshly exposed Zr consumed O_2, our oxygen partial pressure was not under carbon control. However, we do not think that free Zr was present in the cell to reduce the metal oxides (see Fig. 2, $Zr + 2PbO \rightarrow ZrO_2 + 2Pb$). Zr, therefore, acted as a passive inhibitor. Based on Fig. 2, calculations, and oxide layer measurements, we indirectly infer the oxygen potential was between 10^{-24} and 10^{-40} for the 550 °C experiment and 10^{-20} to 10^{-24} for the 650 °C experiment.

2.4. Lead coolant chemistry

Mass transfer of elements from structural metal into the LBE affects the coolant chemistry and governs the LBE attack of the metals tested. If the solubility of the structural materials in the lead is at saturation, further dissolution is limited, mitigating corrosion if temperature and oxygen partial pressure remain constant [14]. Even with our large LBE ratio of 1:30, we still reached saturation levels with several elements in these short-duration experiments.

The solubility of metals in the LBE is a function of temperature. For example, the solubility of Fe in LBE is given by Eq. (2) [16],

$$\log[\mathrm{Fe}] = 6.01 - 4380/T. \quad (2)$$

where T is in K and the solubility [Fe] is in wppm. For operating temperatures of 550 °C (experiment 10), the solubility level of [Fe] in LBE is 5 wppm, whereas for 650 °C (experiment 11) the concentration increases to 18 wppm. Similar relationships hold for Ni, Cr, and Zr, and are provided in Eqs. (3)–(5), respectively.

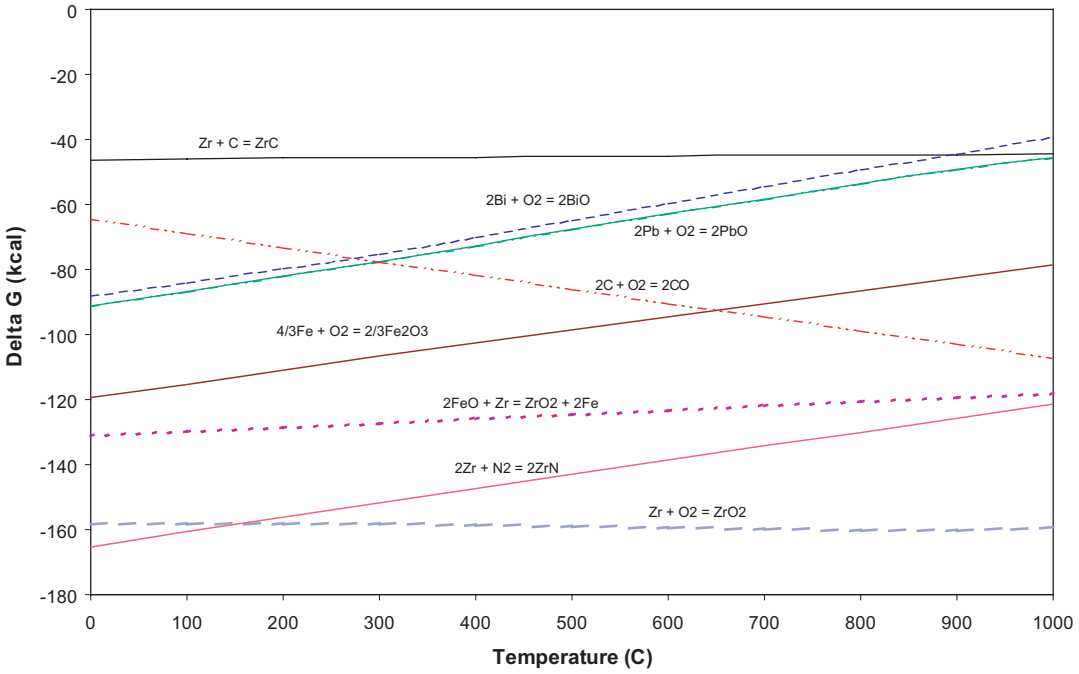

Fig. 2. Modified Ellingham diagram showing the oxidation of the metals present in the system. Note the inverse behavior of the carbon oxidation line.

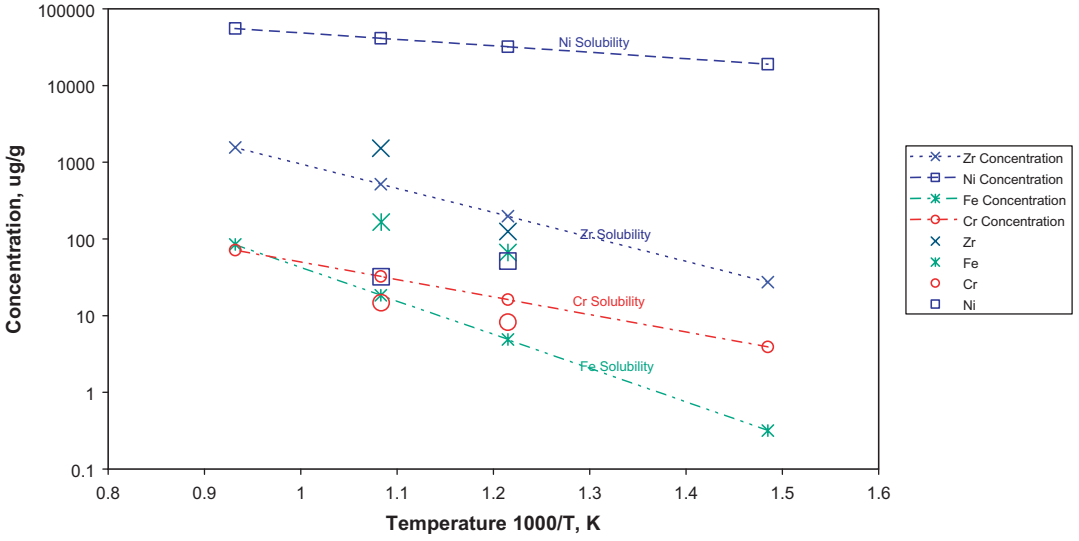

Fig. 3. Theoretical solubility limits of Ni, Cr, Fe, and Zr in LBE as a function of temperature. Overlaid are the measured concentrations of the metals.

$$\log[\mathrm{Ni}] = 5.53 - 843/T, \tag{3}$$

$$\log[\mathrm{Cr}] = 3.98 - 2280/T, \tag{4}$$

$$\log[\mathrm{Zr}] = 6.15 - 3172/T. \tag{5}$$

Lead and dust (captured in the gas handling train) removed at each time step were sent for compositional analysis using an ICP instrument. Fig. 3 presents the ICP data for both experiments and also shows the comparison against the solubility lines generated using Eqs. (2)–(5).

3. Results

The experimental results are summarized with four figures, EDX layer composition of the cross-sections is also presented in each figures. Figs. 4–7 show the interaction layer of HT-9, 410, 316L, and F22 with respect to time and temperature. The two vertical columns are for each temperature; the horizontal columns are for each time step: 100, 300, and 1000 h. This allows easy comparison between temperature and time durations for the interaction layer. The top white layer in all micrographs is the LBE that solidified on the coupon when removed from the corrosion cell. Under the LBE layer is the interaction layer that resides on top of the metal alloy. We also provide trace metal concentration in the LBE as measured by ICP.

3.1. SEM results: thickness of the interaction layer with respect to time

Fig. 4 shows six different SEM cross-section micrographs of HT-9. In the experiment conducted at 550 °C, the thickness growth of the interaction layer is apparent. The results of the experiment conducted at 650 °C also

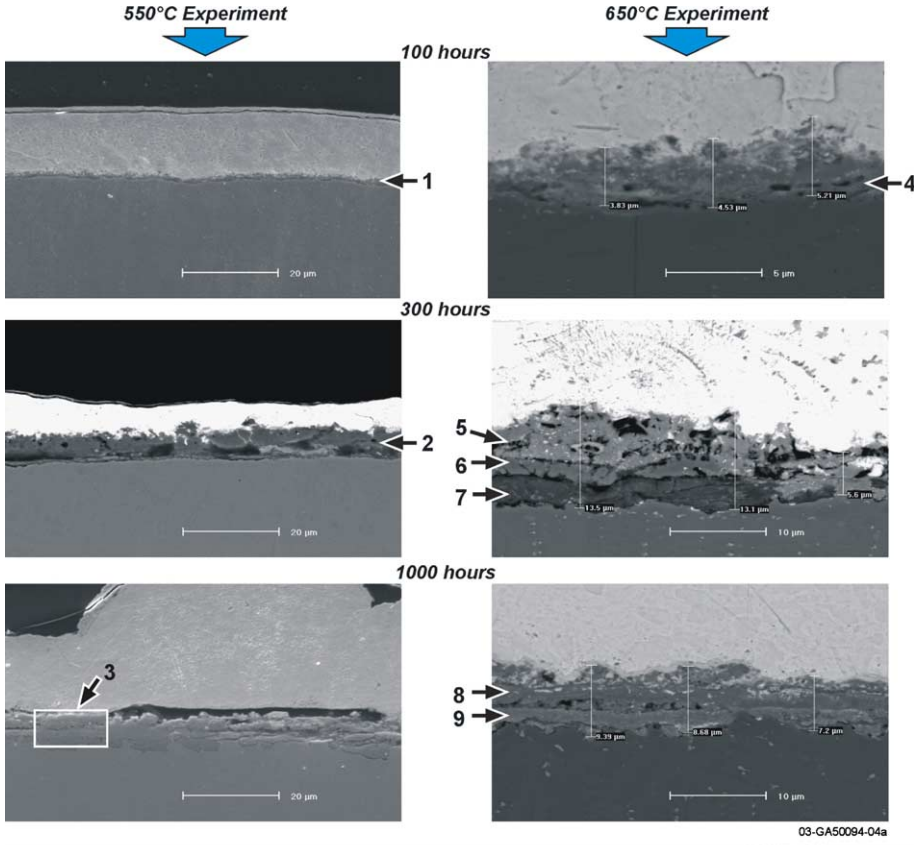

Layer	Temp.	Time	Fe	Cr	W	Pb	Bi	Al	C	Zr	Sr	Ca	Hf	O
1	550°C	100	60.0	5.9	0.9	18.7	13.7	0.5	0.2					
2	550°C	300	63.1	7.7	0.9	2.1	2.6	0.4	0.2					23.2*
3	550°C	1000	66.2	7.4	0.6	1.4	1.1		0.1					23.2*
4	650°C	100	34.9	4.5		22.7	24.3	0.3	0.5	12.0	0.8			
4	650°C	100	28.1	2.0		28.4	29.7	0.2	0.3	10.6	0.8			
5	650°C	300							1.3	73.4			25.3	
6	650°C	300	98.5	1.1					0.1	0.25				
7	650°C	300	79.4	18.0	1.2	0.6			0.1			0.6		
8	650°C	1000	8.2	0.4		28.0	16.0	0.7		36.8			9.9	
9	650°C	1000	29.0	2.2		8.7	20.3	1.5		28.8			8.6	

* An oxygen peak was measured at this location; the values are estimated based on stoichiometry.

Fig. 4. Micrographs of HT-9 cross-sections as a function of exposure time (100, 300, and 1000 h) and exposure temperature (550 and 650 °C). Data normalized wt%.

follows this trend, and there are visible and measurable layers (layers 5 and 8 in Fig. 4) of ZrO_2.

Fig. 5 shows a cross-section of 410, the only alloy to exhibit local pitting at 550 °C and becoming more uniform at 650 °C. Also observable at 650 °C is spalling of the interaction layer, which was Cr-rich, whereas the topmost layer was ZrO_2 (explained in Section 4). In Fig. 6, the micrographs of 316L show the expected interaction layer increasing with respect to time and temperature. In Fig. 7, micrographs of F22 show a large increase of the interaction layer with respect to time for 550 °C, but at 650 °C there was virtually no interaction layer.

Fig. 8 displays the change in the interaction layer at 550 °C of all four alloys as a function of time. In this plot we assume that the interaction layer has not spalled off between time steps. The SEM measurements of the interaction layer of each coupon were averaged together and are plotted with respect to time. Notice that F22 had

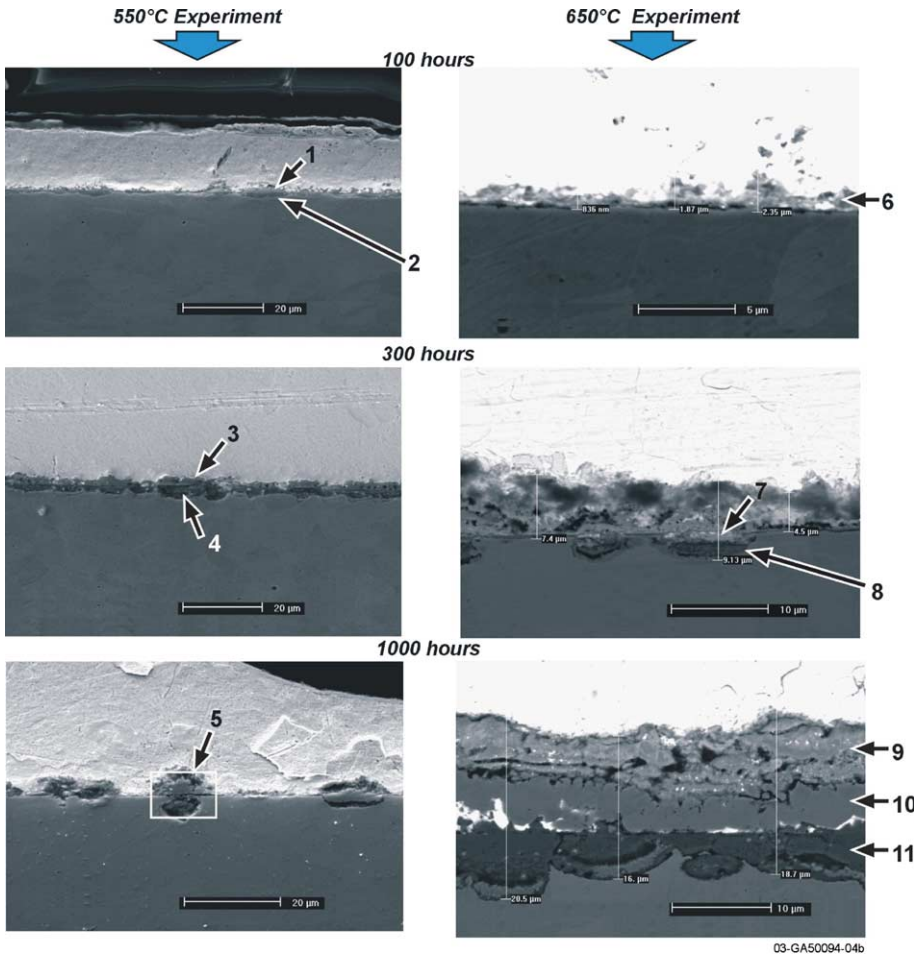

Layer	Temp.	Time	Fe	Cr	Si	Bi	Pb	Mn	O	Al	Na/Ca/Sr	Hf	Zr
1	550°C	100	45.6	0.7	0.9		31.5	0.04	18.9*	2.3			
2	550°C	100	59.2	12.4	0.4	3.4	0.13	0.51	24.0*				
3	550°C	300	53.3	13.1	0.8		4.5	0.51	25.1*	2.7			
4	550°C	300	49.3	18.8	0.6	3.4	1.6	0.53	25.0*	0.7			
5	550°C	1000	47.7	12.2		6.6	7.5		23.2*	1.9	0.96 (Na)		
6	650°C	100	41.1	12.1	0.5	18.6	23.5			2.2	2.0(Re)		
7	650°C	300	14.8			10.0	7.8					14.0	53.4
8	650°C	300	29.9	59.2	0.3	1.0	0.3	5.6			3.6 (Ca)		
9	650°C	1000	2.7			8.7	7.8		21.8*	1.5	0.14 (Sr)	15.5	41.9
10	650°C	1000	92.3	0.90		2.3	3.2						1.3
11	650°C	1000	45.7	24.2	0.6	0.03	1.4	2.4	25.7*				

* An oxygen peak was measured at this location; the values are estimated based on stoichiometry.

Fig. 5. Micrographs of 410 cross-sections as a function of exposure time (100, 300, and 1000 h) and exposure temperature (550 and 650 °C). Data normalized wt%.

the thickest interaction layer, while 316L and 410 had the thinnest interaction layer. Similarly, Fig. 9 displays the change in the interaction layer at 650 °C of all four alloys as a function of time. The interaction layer for F22 was the thinnest, while 316L and 410 grew a thicker interaction layer.

3.2. EDX results: composition of the interaction layer

For all materials, the interaction layer composition was determined by using EDX in the SEM instrument. The distinct compositional data for each layer (as marked by a number) is provided in a table located at the bottom of Figs. 4–7. Some general conclusions for each alloy are:

- Fig. 4 (HT-9): At 550 °C the interaction layer above the substrates are composed of Fe and Cr with some inclusions of Pb and Bi, however, at 650 °C, the inclusions of Pb–Bi in the Fe–Cr increases by a factor of 10. The presence of a ZrO_2 layer is detected.
- Fig. 5 (410): At 550 °C the interaction layer starts as separated pits along the surface that finally (later time steps) coalesce together. The upper portion of the pit has more inclusions of Pb and Bi. At 650 °C, the pitting grows until the entire surface is covered with three distinct interaction layers. The first layer (starting from the 410 substrate) is Cr enriched (24 wt% as compared to 13 wt% in the alloy), the next layer is Cr depleted with Bi and Pb inclusions, and

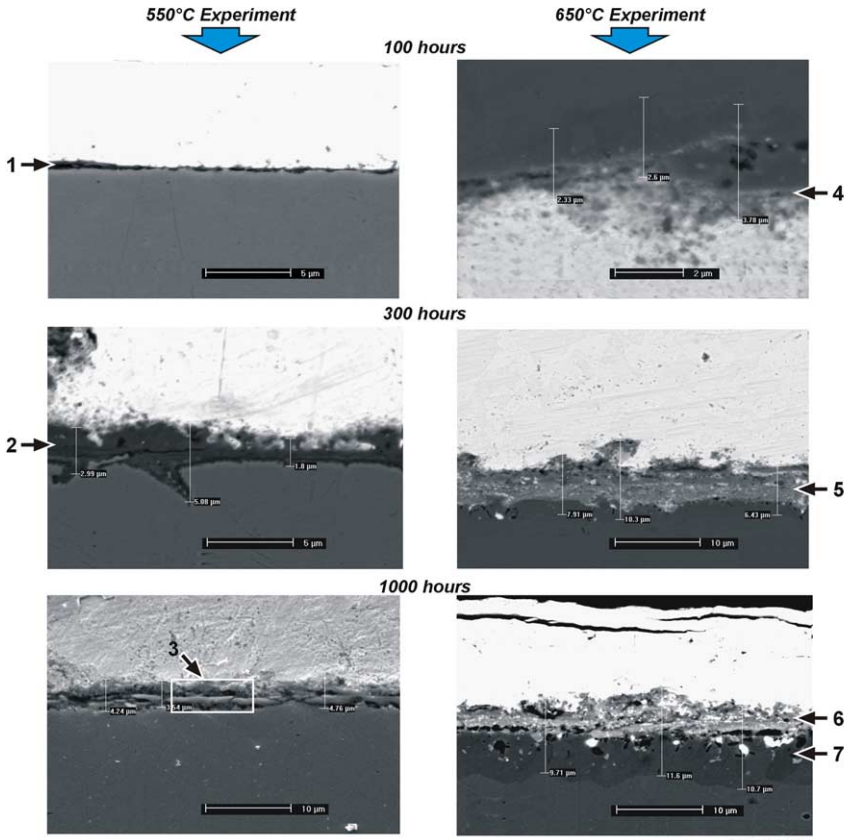

Layer	Temp	Time	Fe	Cr	Ni	Al	O	Si	Pb	Bi	Zr	Sr	Hf	Mo
1	550°C	100	1.8	0.56		0.5			43.6	53.5				
2	550°C	300	64.9	7.6	1.0	1.3	24.4*	0.84						
3	550°C	1000	46.6	18.3	7.4	1.7		10.2	15.7					
4	650°C	100	82.2	8.1					3.35	1.5	4.7	0.19		
5	650°C	300	10.7	1.4		1.4	20.1*	0.17	11.5	22.7	24.0	0.17	8.2	
6	650°C	1000	6.3	0.5		1.2	19.8*		16.3	16.7	30.3		8.8	
7	650°C	1000	61.0	33.3	1.4	0.3		0.24						3.7

* An oxygen peak was measured at this location, the values are estimated based on stoichiometry.

Fig. 6. Micrographs of 316L cross-sections as a function of exposure time (100, 300, and 1000 h) and exposure temperature (550 and 650 °C). Data normalized wt%.

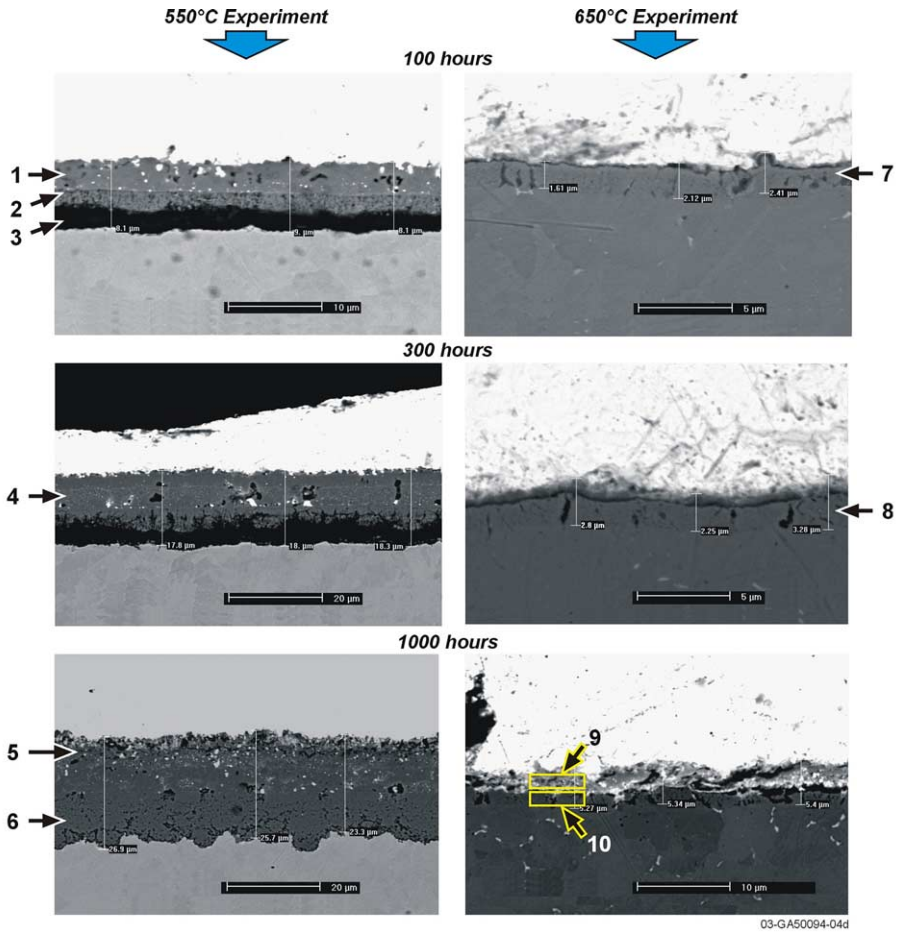

Layer	Temp	Time	Fe	Cr	Pb	Bi	Al	O	Sr	Si	Zr	Mn	Mo	Hf
1	550°C	100	72.5	0.5	2.6	2.1	0.19	21.8*	0.33					
2	550°C	100	66.3	3.6	5.8	1.7	0.29	22.0*		0.3				
3	550°C	100	32.0	1.1	4.4	2.3	25.6	34.0		0.6				
4	550°C	300	73.0	1.6	2.0	0.2	0.27	22.3*	0.44					
5	550°C	1000	76.5			1.3		22.2*			0.10			
6	550°C	1000	73.5	2.7	0.1			22.8*		0.1		0.16	0.64	
7	650°C	100	95.7	2.8	1.6									
8	650°C	300	88.3	3.8	3.3	1.5	0.97				2.2			
9	650°C	1000	36.7	1.4	18.7	13.4	1.41		0.70		21.6			6.0
10	650°C	1000	97.5	1.5			0.35		0.03		0.64			

* An oxygen peak was measured at this location, the values are estimated based on stoichiometry.

Fig. 7. Micrographs of F22 cross-sections as a function of exposure time (100, 300, and 1000 h) and exposure temperature (550 and 650 °C). Data normalized wt%.

the topmost layer is predominately ZrO_2 layer with Pb, Bi and Fe inclusions.

- Fig. 6 (316L): At 550 °C, it is not until 1000 h that the interaction layer has inclusions of Pb and there is Si enrichment. At 650 °C, the interaction layers have a dramatic increase of Zr with inclusions of Pb and Bi. At 1000 h layer (7) appears to be growing into the substrate resulting in Si depletion and Cr enrichment.
- Fig. 7 (F22): At 550 °C, distinct layers are visible containing inclusions of Pb and Bi. The EDX detected a strong O_2 peak for all the layers indicating oxidation of the metal surface. At 650 °C, the ZrO_2 layer is present, which seems to inhibit the oxidation of the substrate surface and the inclusions of Pb and Bi.

Overall, at 550 °C, the interaction layers produced were as expected – increasing in thickness and inclusions with

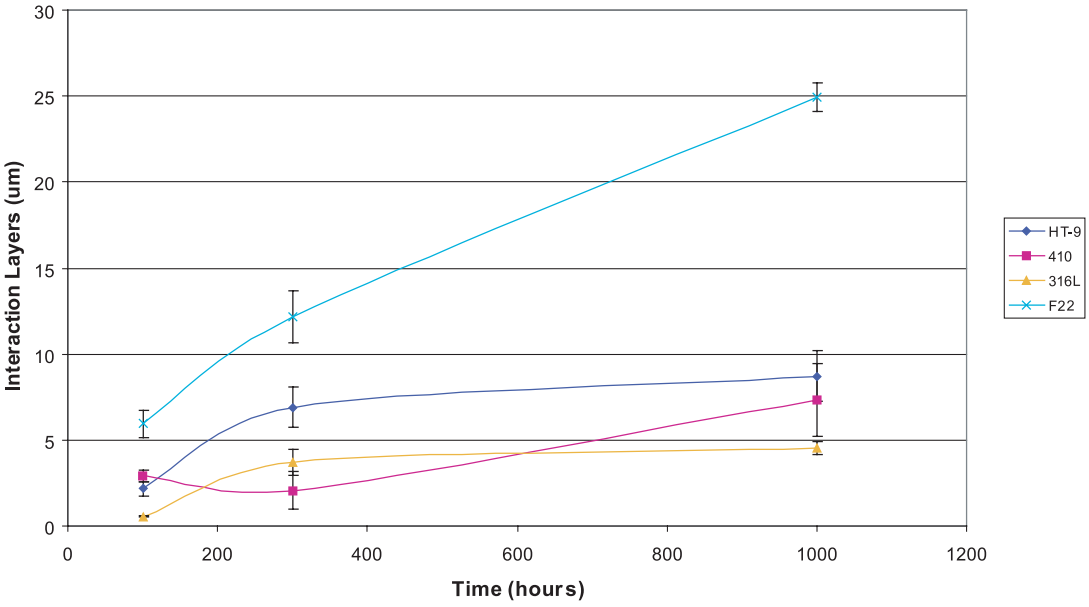

Fig. 8. Interaction layer growth as a function of time at an exposure temperature of 550 °C.

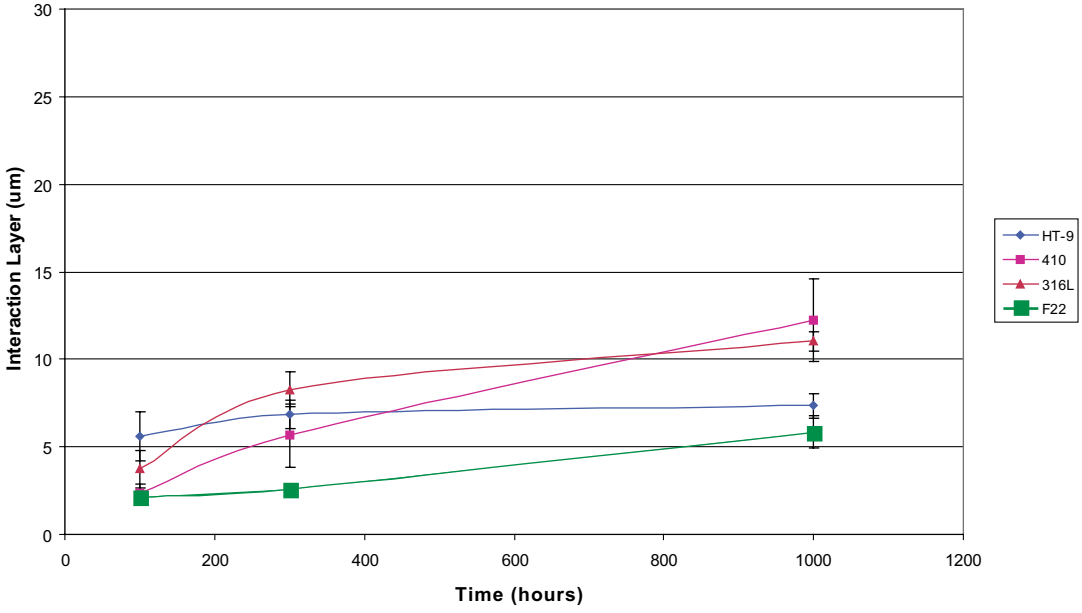

Fig. 9. Interaction layer growth as a function of time at an exposure temperature of 650 °C.

time. At 650 °C, the presence of ZrO_2 as the top interaction layer complicated the formation of the interaction layer and this mitigated the growth on the F22. Oxygen detection in the interaction layer is difficult with the SEM where a strong peak in the spectrum was observed we reported the calculated stoichiometric amount.

3.3. Coolant chemistry

LBE samples were extracted at each time step for ICP analysis to quantify the elemental concentration of Fe, Cr, Ni, and Zr present in the LBE. The Zr appeared as a result of spalling-off of the ZrO_2 layer formed in the

Table 2
Calculated versus measured solubility at 550 and 650 °C

Element	Cal 550 °C[a]	Cal 650 °C[a]	Mass 550 °C[b]	Mass 650 °C[b]	% of dissolved 550 °C[c]	% of dissolved 650 °C[c]	ICP 550 °C[d] (average)	ICP 650 °C[d] (average)
Fe	4.89	18.42	0.12	0.45	0.05	0.20	66.41	166.39
Cr	16.22	32.37	0.40	0.79	1.3	2.6	8.20	14.71
Ni	32 000	41 400	784	1014	14 500	19 900	51.4	32
Zr	198	518	4.9	13	3.0	7.9	116.1	1576

[a] Solubility limit of each material in ppm.
[b] Mass of each material in grams required to reach the solubility limit.
[c] Percentage of the material in the cell required to dissolve in order to reach the solubility limit.
[d] Average amount of material in solution as measured by ICP (ppm).

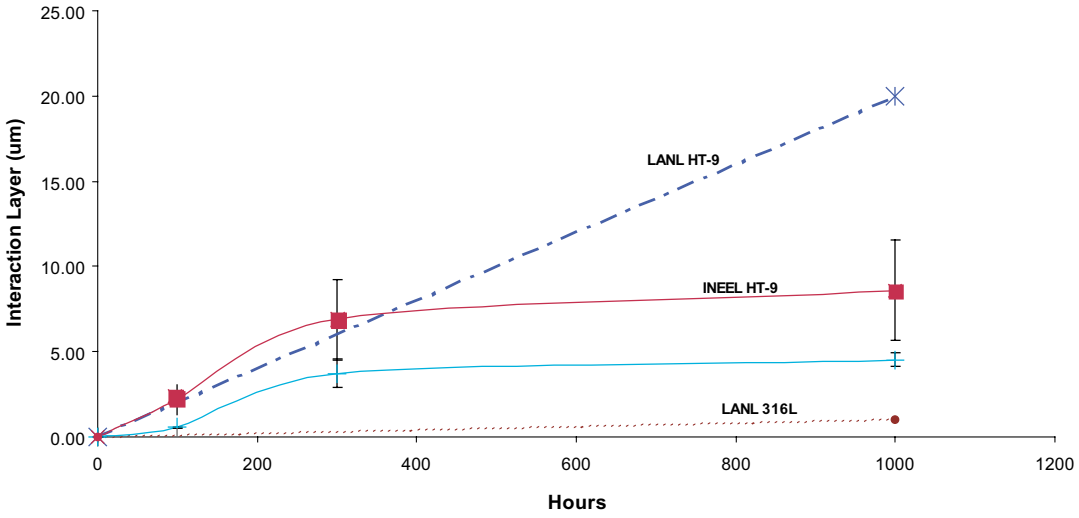

Fig. 10. Comparison of corrosion rates of 316L and HT-9 measured in a non-isothermal loop, to the interaction layer growth in an isothermal test cell.

beginning of the experiment. The results of ICP analysis are provided in Table 2 along with the calculated solubility levels. The first two columns are the theoretical solubility of the elements in the LBE. The next two columns are the mass of each element inserted into the system, and the following two columns are the percent of each element that dissolved into the system. The last two columns are the averaged amounts of each material in solution, as measured by ICP. Fig. 3 shows the concentration of each element in the LBE compared to their theoretical solubility limits. At 550 °C, nickel has the highest solubility in LBE (5000 wppm at 2 wt%), followed by Cr and Fe (~500 wppm at 0.2 wt% and ~2.5 wppm at 10^{-3} wt%, respectively).

In a non-isothermal system, transport of material in solution from a higher temperature region to a lower temperature region will result in precipitation of dissolved metallic contaminants in the cooler regions of the system – mass transfer corrosion. The experiments reported in this paper were conducted in an isothermal loop resulting in a saturated amount of metals in the LBE, which reduces the mass transfer and therefore does not exactly correspond to a LBE cooling system. Fig. 10 provides a comparison of our data (isothermal) to the Los Alamos corrosion data obtained at the flowing LBE loop facility at Obninsk, Russia [17].

4. Discussion

The pre-oxidized zirconium corrosion cells resulted in gas phase chemistry that affected LBE corrosion in the loop. The Zr appeared in LBE as a result of spalling-off of the protective ZrO_2 layer formed in the beginning of the experiment. The gas phase measurement data showed complete removal (below the instrument detection level) of oxygen and a reduction in nitrogen concentration. The inert argon gas used to induce LBE flow

in the cell contained trace amounts of N_2, 100–200 vppm; O_2, 70–100 vppm; and H_2, 1–10 vppm. In the 550 °C experiment, the pre-formed ZrO_2 layer inside the corrosion cell suffer less degradation, as evidenced of the Zr concentration in the LBE being 37% below the saturation level. However, in the higher temperature experiment, the ZrO_2 layer was sloughing off into the bath, resulting in excess ZrO_2 (above the saturation point) of 295%, calculated by Eq. (5). This resulted in thermodynamically favorable reactions of Zr with O_2 and N_2, shown in Fig. 2 to be more prevalent due to kinetics (higher temperature) and mass transfer (exposing fresh Zr as the oxide layer sloughed off). Thus, the zirconia in the LBE prevented the growth of the interaction layer (magnetite layer) by forming a layer of zirconium compounds (we suspect both oxide and nitrides of zirconium) on the surface. Similar behavior has been previously confirmed in bismuth [18].

5. Conclusions

The behavior of F22, HT-9, 316, and 410 iron alloys in LBE has been studied in an isothermal zirconium piping loop system over the temperature range of 550–650 °C at a fluid velocity of 0.4 m/s. The zirconium in LBE inhibited the growth of the interaction layer by consuming oxygen and nitrogen in the system, thus changing the solubility of the elements in the LBE. At higher temperatures, a layer of zirconium compounds (oxides and nitrides) prevented the alloys from dissolving into the LBE. However, this layer did not seem to be tightly adhered and is liable to spall off. No detailed conclusion can be drawn concerning the influence of carbon on oxygen potential when zirconium is present. Future experiments will be replicated in an iron-based alloy corrosion cell.

Acknowledgements

The authors express their appreciation Todd Morris, Sue Watkins, and Kyle Burch in providing analytical support. The work was supported through the INEEL Long-Term Research Initiative Program under DOE Idaho Operations Office Contract DE-AC07-99ID13727 and the DOE-NE student fellowship program.

References

[1] H. Glasbrenner et al., J. Nucl. Mater. 296 (2001) 237.
[2] G. Muller et al., J. Nucl. Mater. 301 (2002) 40.
[3] J. Knebel, G. Muller, J. Konys, ICONE 10, Arlington, 14–18 April 2002.
[4] P.F. Tortorelli, O.K. Chopra, J. Nucl. Mater. 103&104 (1981) 621.
[5] G. Benamati et al., J. Nucl. Mater. 301 (2002) 23.
[6] J.A. James, J. Trotman, J. Iron, Steel Inst. (1960).
[7] A. Taskinen, Scand. J. Metall. 8 (1979) 185.
[8] O. Chopra et al., Fusion Technol. 8 (1985) 1956.
[9] A.J. Romaro, et al., Brookhaven National Laboratory Technical Report, BNL811(T-313), 1963.
[10] J.R. Weeks, A.J. Romano, Corrosion 25 (1969) 131.
[11] E.P. Loewen, P.E. MacDonald, ANS Paper A0517, 2000.
[12] E.P. Loewen, P.E. MacDonald, ANS Paper B0517, 2002.
[13] G. Muller, G. Schumacher, F. Zimmermann, J. Nucl. Mater. 278 (2000) 85.
[14] N. Li, J. Nucl. Mater. 300 (2002) 73.
[15] C.H. Lefhalm, J.U. Knebel, K.J. Mack, J. Nucl. Mater. 296 (2001) 301.
[16] X. He, N. Li, M. Mineev, J. Nucl. Mater. 297 (2001) 214.
[17] N. Li, X. He, Proc. ANS Topic. Meet., Nuclear Applications of Accelerator Technology, Reno, NV, USA, 11–15 November 2001.
[18] G.W. Horsley, J.T. Maskrey, J. Inst. Met. 86 (10) (1958) 446.